Algorithm for continual monitoring of fog ~~life cycles~~ based on geostationary satellite imagery ~~as a basis for solar energy forecasting~~

Babak Jahani[1,2,3], Steffen ~~Karalus[3]~~Karalus[4], Julia Fuchs[1,2], Tobias ~~Zech[3]~~Zech[4], Marina Zara[1,2], Jan Cermak[1,2]

[1]Institute of Meteorology and Climate Research, Karlsruhe Institute of Technology (KIT), Karlsruhe, Germany.
[2]Institute of Photogrammetry and Remote Sensing, Karlsruhe Institute of Technology (KIT), Karlsruhe, Germany.
~~[3]Fraunhofer~~[3](now at) SRON Netherlands Institute for Space Research, Leiden, the Netherlands.
[4]Fraunhofer Institute for Solar Energy Systems ISE, Freiburg, Germany.

Correspondence to: Babak Jahani (~~babak.jahani@kit.edu; b.jahani@sron.nl~~b.jahani@sron.nl); Jan Cermak (jan.cermak@kit.edu)

1

Abstract. ~~Detection and monitoring of fog and low stratus (FLS) is particularly important in the context of photovoltaic power production, as FLS, unlike moving clouds, can persist longer and impact larger regions simultaneously, making regional power grid balancing harder. Although photovoltaic power production is limited to daytime hours, its short term forecasting (especially during the early hours of the day) in the context of high PV penetration systems grid operation, benefits from a complete knowledge of FLS life cycle. As this life cycle usually begins at night and ends during the day, a day night consistency in the algorithms used for monitoring FLS is required.~~ This study presents an algorithm for detection of FLS over Europe based on the infrared bands of the SEVIRI (Spinning Enhanced Visible and InfraRed Imager) instrument onboard the Meteosat ~~second generation~~Second Generation geostationary satellites. As the method operates based on the SEVIRI infrared observations only, it is expected to be stationary in time and thus can provide a coherent and detailed view of FLS development over large areas over the 24H day cycle. The algorithm is based on a gradient boosted trees machine learning model that is trained with ground truth observations from Meteorological Aviation Routine Weather Reports (METAR) stations and the SEVIRI observations at bands cantered at 8.7, 10.8, 12.0 and 13.4 μm wavelengths. The METAR data used here ~~comprises~~comprise a total number of 2,544,400 datapoints spread over the winters (i.e., ~~1st of~~1 September to ~~31st of~~31 May) of the years 2016-2022 and 356 locations across Europe. Among them, the datapoints corresponding to 276 stations and the winters of 2016-~~018~~2018 and 2019-2021 (~45% of all datapoints) were used to train the algorithm. The remaining datapoints comprise four independent datasets which were used to validate the algorithm's performance and applicability to ~~the~~ time spans and locations ~~in~~within the study area (i.e., Europe) that extend beyond ~~particular locations and time spans~~those covered by the datapoints used for ~~training~~ the algorithm~~. Additionally,~~ training. Also to compare the algorithm's accuracy at the locations of METAR stations with that of the ~~stablished~~established state-of-the-art daytime FLS detection algorithm Satellite-based Operational Fog Observation Scheme (SOFOS). Validation of the algorithm against the METAR data, showed that the algorithm is well suited for detection of FLS. Specifically, the algorithm is found to detect FLS with probabilities of detection (POD) ranging from 0.70 to 0.82 (for different inter-comparison approaches), and false alarm ratios (FAR) between 0.21 and 0.31. These numbers are very close to those achieved by SOFOS for ~~discriminating the~~differentiating FLS from other sky conditions at the tested locations and time spans. These results also showed that the technique's applicability in the study region extends beyond the particular locations and time spans covered by the datapoints used for training the algorithm.

1 Introduction

Fog and low stratus (FLS) are both persistent aggregations of water particles in liquid and/or solid phases, i.e., clouds close to the Earth's surface. As the cloud-_base-_height is the only real difference between the two (fog: touching the ground; low stratus: above ground), they are frequently treated together as a single category from the satellite perspective (i.e., FLS). FLS influences various aspects of life on the Earth: on the one hand it may act as source of water supply (e.g. ~~Lehnert et al., 2018; Shanyengana et al., 2002~~Lehnert et al., 2018; Shanyengana et al., 2002), as well as a modifier in the global climate system (Vautard et al., 2009). On the other hand, it causes large economic costs in transport, health and energy sectors (Köhler et al.,

2

Formatted: Centered

2017; Pérez-Díaz et al., 2017). For these reasons, continuous (and ideally near real-time) detection of FLS and monitoring of
its spatiotemporal patterns and developments is ~~of~~ essential ~~importance. One~~. An important application lies in ~~the usage~~ solar
energy usage. With the rising share of electricity generated from photovoltaic (PV) systems, the prediction of current and
future solar irradiance and, hence, PV power output becomes crucial for the operation of modern power grids. In the context
of PV power production, detection and monitoring of FLS is particularly important as FLS, unlike moving clouds, can persist
longer and impact larger regions simultaneously, making regional power grid balancing a challenging task.

Geostationary satellites have an outstanding potential for detection and monitoring of FLS. That is because they continuously
scan the Earth from the same angle over the 24H of the diurnal cycle, ~~thus~~ providing spatiotemporally coherent spectral images
of the Earth. To exploit this potential, to this day several FLS detection methods have been developed and applied (e.g., ~~Cermak & Bendix, 2007, 2008; Egli et al., 2018; Ellrod, 1995; Nilo et al., 2018; Underwood et al., 2004~~Cermak & Bendix, 2007, 2008; Egli et al., 2018; Ellrod, 1995; Nilo et al., 2018; Underwood et al., 2004), which detect FLS by performing a sequence of
spectral and/or spatial tests on ~~the~~ satellite measurements. Although these methods have proven to be useful exploring the FLS
characteristics (e.g., ~~Cermak et al., 2009; Egli et al., 2017; Pauli, Cermak, & Andersen, 2022; Pauli, Cermak, & Teuling, 2022~~Cermak et al., 2009; Egli et al., 2017; Pauli, Cermak, & Andersen, 2022; Pauli, Cermak, & Teuling, 2022), they usually
consist of solar zenith angle dependent, as well as separate daytime and nighttime schemes, making use of spectral channel
characteristics particular for either night or day. This, however, makes the continuous monitoring and forecasting of FLS life
cycle and occurrence at the critical of the day (i.e., sunrise) impossible. For example, ~~a~~an FLS detection method may operate
based on ~~the~~ shortwave reflectances, as FLS ~~-~~covered regions typically have high reflectivity and smooth texture in the visible
spectral region (Lee et al., 2011). But as no reflectance data is available during nighttime, a whole other algorithm ~~will~~would
be required to be applied over nighttime. FLS can also be detected by testing the difference between the brightness temperatures
in Medium- (MIR) and Long- (LIR) ~~wavelength~~wave Infrared bands (typically referred to radiation at wavelengths between
3-8 and 8-15 μm, respectively) against threshold values. That is because ~~as~~ the FLS droplets are typically smaller than those
of other cloud types. As a result, ~~for them, the~~FLS shows a greater contrast between the ~~emissivities~~brightness temperatures
measured at MIR and LIR bands ~~is greater,~~ compared to other clouds (Hunt, 1973). However, as MIR has a solar component
during daytime, application of this technique requires daytime and nighttime separation. ~~A stable~~To overcome this limitation
and enable consistent FLS detection across the entire diurnal cycle, an approach ~~applicable during day and night would have~~ that relies solely ~~depend~~ on observations ~~at~~in the LIR bands. ~~As a complete knowledge of FLS event development in space and time is needed as a basis for short-term forecasting, e.g. in the context of grid operation (in case of high PV penetration systems), the~~ would be required.

The main objective of the present study is to develop and validate a single fully diurnal FLS detection algorithm for Europe
based on geostationary satellite observations. The guiding hypothesis of the present study is that FLS can be discriminated
from cloud-free regions and non-FLS clouds based on spectral LIR data with an accuracy comparable with the existing state-
of-the-art daytime FLS detection algorithms.

Formatted: Centered

Satellite detection of FLS using only LIR bands only is a quite challenging task and historically believed to be a rather impossible one ~~(Güls & Bendix, 1996). That is mainly because as FLS emit~~(Güls and Bendix, 1996). That is mainly because FLS emits at temperatures very close to that of the Earth's surface. Nonetheless, ~~Andersen & Cermak (2018) succeeded~~Andersen & Cermak (2018) succeeded at developing a method for FLS detection over the Namib desert (located in Southern Africa) which operates solely based on the brightness temperatures measured at the LIR bands of the Spinning Enhanced Visible and InfraRed Imager (SEVIRI) sensor on board the Meteosat Second Generation (MSG) spacecraft. Specifically, they discriminated FLS from cloud-free land by analysing the spatial structure (texture) of images constructed from the ~~difference~~differences between the brightness temperatures measured at 12.0 and 8.7 μm SEVIRI channels. The main underlying assumptions associated with this method are i) the 12.0-8.7 μm values are typically greater for clouds than for land surface, and ii) the 12.0-8.7 μm calculated for bare soil shows a higher level of spatial heterogeneity compared to ~~that of the~~ smooth FLS top surfaces ~~of FLS. Their success in developing their algorithm shows that~~. Andersen & Cermak (2018) showed that, although small, there are distinct differences between the spectral signatures of a clear~~-~~ land and FLS in the LIR region, which makes ~~it~~their distinction possible ~~to distinguish them from each other~~. Nevertheless, this method is applicable to regions where the mentioned assumptions are met (i.e., deserts and possibly arid regions) and cannot be easily ~~ported~~extrapolated to the much more complex geo- and atmospheric conditions of Europe. Therefore, to this date, no approach for the continual~~,~~ 24H detection of FLS over Europe exists.

This study presents and validates a single machine-learning (ML) algorithm for detection of FLS over land across Europe, based on Meteosat-SEVIRI bands ~~cantered~~centered at 8.7, 10.8, 12.0 and 13.4 μm wavelengths. Furthermore, it provides an intercomparison between the accuracy of this method and that of the established state-of-the-art daytime FLS detection algorithm Satellite-based Operational Fog Observation Scheme (SOFOS; ~~Cermak, 2006; Cermak & Bendix, 2008).~~Cermak, 2006; Cermak & Bendix, 2008) to address the objectives of the study. The method presented here is based on a gradient boosted trees (XGBoost) ML model that is trained with observations from METeorological Aviation routine weather Reports (METAR) stations and the LIR observations of SEVIRI on board Meteosat-10 and Meteosat-11 platforms. As the method presented here operates solely based on the spectral data in the LIR region, it is expected to be applicable during the 24H of the diurnal cycle over European lands. Thus, it is suitable for continuous monitoring of FLS over Europe and can reveal a detailed view of the diurnal and spatial patterns of FLS over Europe. This can be of essential value for analysis of FLS occurrence and related processes as well as improvement of methods for PV power forecasting. It can also serve as a precondition for statistics-based nowcasting.

2 Data ~~and Methods~~

2.1 Satellite observations

SEVIRI is a multi-purpose scanning (passive) radiometer onboard MSG geostationary satellites operated by the European Organization for Exploitation of Meteorological Satellites (EUMETSAT; Aminou, 2002). This instrument has been in

4

Formatted: Centered

operation by EUMETSAT at 0° latitude and longitude at the altitude of ~35800 km above mean sea level since early 2004 and

110 is intended to remain in service at 0° until 2033 (expected lifetime of the last MSG mission, i.e., Meteosat-10). SEVIRI measures upwelling radiance at the top of the atmosphere (TOA) for the Earth's whole disk covering Europe, the North Atlantic, and Africa in 12 spectral channels in 15-minute intervals (12 minutes scanning time followed by 3 minutes of processing time). Eleven of the SEVIRI channels are narrow-band channels which are spread over the spectral region between 0.56 (visible) to 14.4 (LIR) μm and have a sampling spatial resolution of ~~3x3 km~~3×3 km^2 at nadir ~~(they are referred to as low~~

115 ~~resolution channels).~~. The remaining one is a broadband High Resolution Visible channel (0.6 - 0.9 μm~~; referred to as HRV~~) with a sampling resolution of 1 km at nadir. The level-1.5 product of SEVIRI ~~(Hanson & Mueller, 2004; Schmetz et al., 2002; Tranquilli et al., 2016)~~(Tranquilli et al., 2016; Hanson and Mueller, 2004; Schmetz et al., 2002) consists of geolocated, radiometrically pre-processed TOA upwelling radiances observed by SEVIRI (spacecraft specific effects have been removed) at its 12 channels. ~~For the present study, the level 1.5 radiances measured by SEVIRI instruments at 0 degree at channels~~

120 ~~centered at 0.6, 0.8, 1.6, 3.9, 8.7, 10.8, 12.0 μm wavelengths were utilized. This data was acquired from EUMETSAT for~~ ~~region covering Europe and north Africa and includes the winter periods (i.e., spans 1st of September to 31st of~~The present study uses the level 1.5 radiances measured by MSG-SEVIRI instruments positioned at 0° latitude and longitude. The data includes measurements from channels centered at 0.6, 0.8, 1.6, 3.9, 8.7, 10.8, 12.0 μm wavelengths. This data was acquired from EUMETSAT (EUMETSAT, 2017) for region covering Europe and north Africa and includes the winter periods (i.e., 1

125 September - 31 May) between the years 2016 and 2022. This data was measured by the SEVIRI instruments onboard MSG-3 and MSG-4 platforms. The acquired data was ~~then~~ calibrated and converted to ~~reflectance~~reflectances (ρ; for 0.6, 0.8, 1.6 μm channels) and brightness ~~temperature~~temperatures (BT; for 3.9, 8.7, 10.8, 12.0 and 13.4 μm channels) following the procedure explained in ~~(EUMETSAT, 2017)~~EUMETSAT (2017) using the satpy python package (Martin et al., 2021). The summer months (i.e., June, July, and August) were excluded from the analysis because the FLS occurrence frequency is very low over

130 these months (Egli et al., 2017) and their inclusion in the analysis largely affects the imbalance between the observed FLS positive and negative cases (see Table 1 for more information).

2.2 SOFOS

As a reference for the newly developed algorithm, the well-established and well-validated satellite-based the Operational Fog Observation Scheme (SOFOS, Cermak 2006, Cermak & Bendix 2008) was used. A daytime-only technique, this approach

135 was developed specifically for MSG SEVIRI, and makes use of the visible, mid-infrared and thermal infrared channels in a series of threshold tests. These include per-pixel spectral tests as well as tests applied on spatially coherent and distinct areas of pixels.

2.3 Ground-based observations

The METAR (METeorological Aviation Routine Weather Reports) comprise the reports of weather measurements performed

140 at a network of meteorological stations located at ~~the~~ airports across the world. The primary objective of these measurements

5

is aviation safety, but they also have an application in meteorology. The METAR parameters cloud base height (CBH; m), sky cloud cover (CC; okta) and horizontal visibility (HV; km) for the period 1 September 2016 to 31 May 2022 were acquired and used in the present study to identify the FLS conditions based on ground-based observations. These parameters are retrieved either automatically (instrumentation is not standardized) or estimated by human observers at each station at temporal frequencies of 1 hour or less. The temporal frequency of the observations performed at these stations is related to the weather conditions, airport size and traffic. In particular, stations located at large and busy airports are equipped with automatic devices and tend to have a higher frequency of observations compared to small airports. Also, under weather conditions violating flight safety such as fog occurrence or extreme weather, the frequency of the observations at these stations is increased to ensure flight safety.

The acquired data was first subjected to a quality control procedure to filter out the stations with unreliable observations. Specifically, the stations not meeting at least one of the following conditions were considered unreliable and were discarded from the analysis: 1) average number of observations per hour greater than 1.5 for the data period, 2) average number of empty observations less than 0.05 during the data period, or 3) continuous data gaps less than one month. The underlying assumption for defining these tests is that the data from stations with rather homogeneous frequency of observations is more likely to have reliable accuracy and consistency. The quality control thresholds applied here have been defined empirically as such being restrictive enough to filter out the stations with unreliable observations, and yet relaxed enough to get a reasonable number of temporally homogeneous observations for further analysis. By applying the abovementioned filters, 591 out of 947 stations were discarded. The locations of the remaining 356 stations were spatially matched with the SEVIRI grid using the smallest distance between the center of each SEVIRI pixel and the station location. For the temporal matching, the METAR times of observation were first rounded up to the closest 15-minute intervals (t_m) of SEVIRI. Then, the SEVIRI images with the timestamps t_m+15minute were considered as the temporally matched images, as the actual SEVIRI scanning time for the study area is much closer to the end of each 15-minute interval. The location of these stations is illustrated in Figure 1. As can be inferred from this figure, the stations selected are spread across Europe (plus four in north Africa), covering a wide range of regions with various surface types, altitudes, and meteorological conditions.

6

Elevation above mean sea level (m)

Formatted: Centered
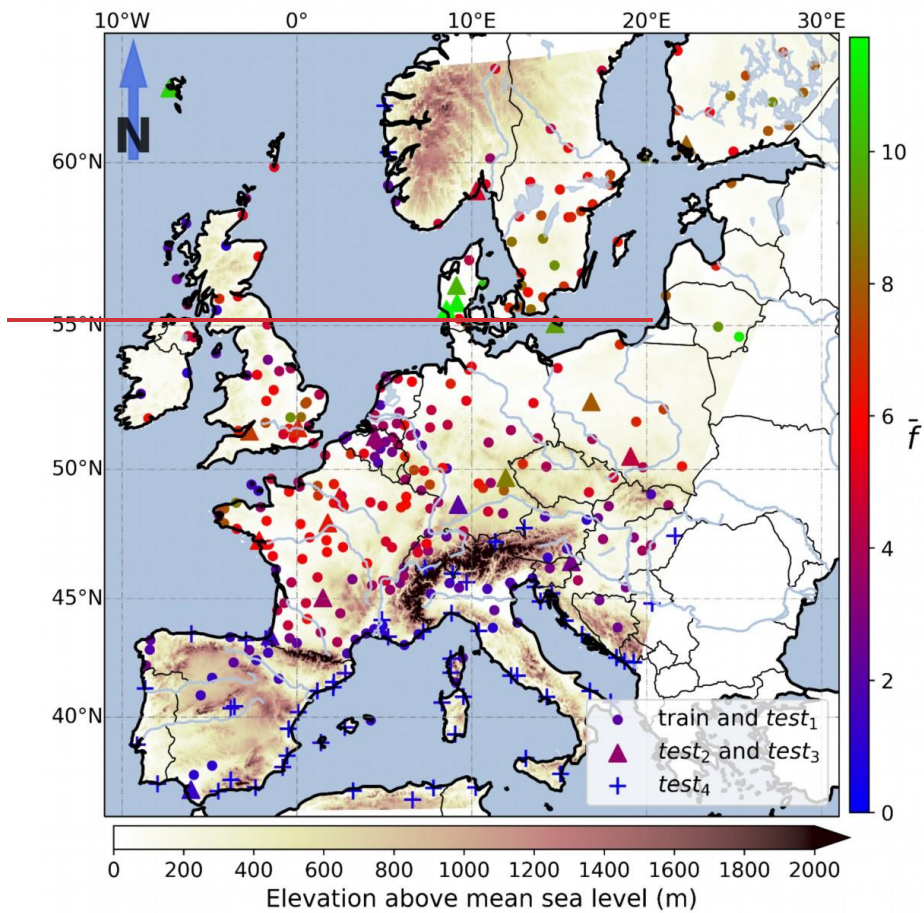
Figure 1. Geographical location of the selected ground observation (METAR) sites. The horizontal color bar indicates the elevation above mean sea level for the study area (m; obtained from EUMETSAT ~~Satellite Application Facility on Land Surface Analysis~~: last access: 16.01.2023 - 13:36 GMT+1). The filled circles show the geographical locations of the stations included in the "~~train~~training" and "$test_1$" datasets. The triangles illustrate the geographical locations of the stations included in the datasets "$test_2$" and "$test_3$", (see Sect. 2.4 for more information). The locations of the stations included in test4 dataset are shown with plus ("+") signs. The vertical color bar indicates the mean annual FLS occurrence freque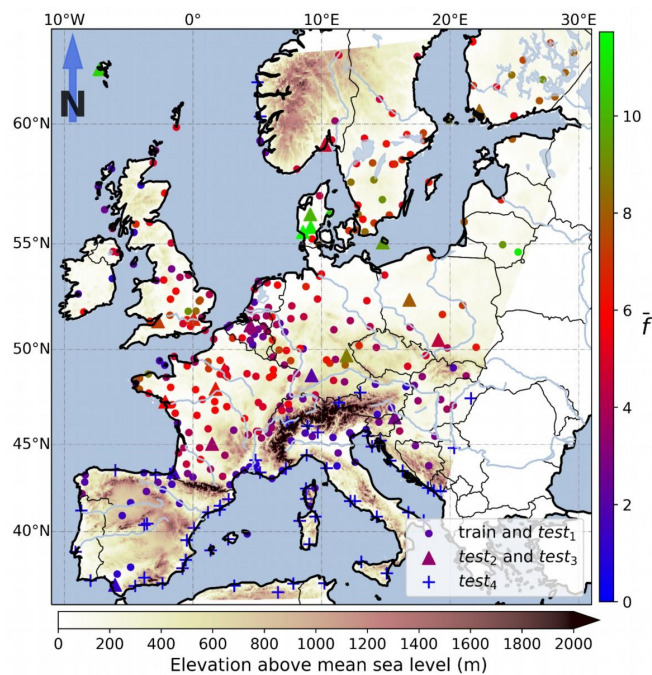ncy ($\bar{f}$~~)~~: %) at the location of the station as ~~indicated according to the procedure explained~~described in Sect. 2.4 of the manuscript based on the modified ground-based FLS labels (before selecting the confident labels).

~~2.~~3 ~~SOFOS~~

~~As a reference for the newly developed algorithm, the well-established and well-validated satellite-based the Operational Fog Observation Scheme (SOFOS, Cermak 2006, Cermak & Bendix 2008) was used. A daytime-only technique, this approach was developed specifically for MSG SEVIRI, and makes use of the visible and mid-infrared and thermal infrared channels in a series of threshold tests. These include per-pixel spectral tests as well as tests applied on spatially coherent and distinct areas of pixels.~~

2.4 Methods

3.1 FLS labels

185 ~~The~~The present study uses the ground-based identified FLS occurrences as the basis for algorithm development and validation purposes. The FLS occurrences were identified using the CBH, CC and HV measurements performed at the ~~locations of the~~ selected METAR stations ~~were used for the ground-based identification of FLS occurrences. To this aim, the case of fog and homogeneous~~ (see section 2.2 for more information). Fog was defined by HV values below 1 km, and low stratus ~~conditions were first determined separately and then the two were combined to produce the ground-based FLS labels. Specifically, the~~

190 ~~data points with HV less than 1 km were labelled as fog and those with~~by CBH ~~of the lowest cloud layer less than~~below 1 km and CC ~~greater than~~above 5 ~~octas were labelled as homogeneous low stratus conditions~~oktas (Egli et al., 2017). ~~The data points for which~~Then, Observations with either fog or low stratus ~~was observed~~ were ~~labelled as~~ marked "*FLS-positive*. ~~Data pints with no reported values for at least one of the parameters*"*,~~" while those missing HV, CBH, or CC data were ~~labelled as~~ marked "*undefined*. ~~Data points for which*"*.~~ Observations with neither fog nor low ~~status was observed~~stratus were labelled ~~as~~ "*FLS-*

195 *negative-.*".

The FLS labels produced this way indicate whether FLS is ~~observed~~detected from the perspective of ground-based observer/instrument. However, these labels may not be consistent with what is ~~seen~~observed from ~~the~~ space, as the satellite's field of view (FOV) may be ~~blocked by~~ contaminated with layers of non-FLS clouds ~~passaging~~passing through its line of sight (LOS). ~~Another issue~~This is ~~that the~~particularly relevant in Europe, where about 30% of FLS events are obscured by other

200 clouds (Cermak, 2018). Additionally, the "*FLS-negative*" labels indicated ~~as~~above, do not specify the sky condition (cloudy or cloud-free- land) in the satellite's FOV. To cope with these two issues, the non-FLS clouds blocking the satellite's LOS were identified using the SEVIRI spectral measurements. Particularly, a series of spectral tests were performed using the collocated SEVIRI $\rho_{0.6}$, $\rho_{1.6}$, $BT_{3.9}$, $BT_{8.7}$, $BT_{10.8}$, $BT_{12.0}$ and $BT_{13.4}$ data corresponding to each data point. These tests are the same those used in the SOFOS algorithm for classification of the SOFOS classes "water", "Cirrus" and "ice" clouds ~~(Cermak~~

205 ~~& Bendix, 2008) and can rather confidently discriminate non-FLS clouds from FLS and cloud-free land. Afterwards, the abovementioned FLS labels were modified according to the non-FLS cloud observations as follows: among the data points labelled as FLS negative based on the ground data, those which were non-FLS-cloud-free and non-FLS-cloud covered based on the SEVIRI data were classified as "clear-sky" and "non-FLS-cloud" conditions, respectively. As for the data points which were labelled as FLS positive, those identified as non-FLS-cloud-free and non-FLS-cloud covered were classified as "FLS"~~

210 ~~and "multi-layer" (FLS under a non-FLS cloud) conditions, respectively.~~(Cermak and Bendix, 2008) and can discriminate non-FLS clouds from FLS and cloud-free land.

The ground-based FLS labels were updated based on the above-mentioned tests performed on the SEVIRI data as follows: FLS-negative observations from ground data were classified as "clear-sky" if no non-FLS clouds were detected, and as "non-FLS-cloud" if clouds were present. For FLS-positive points, those with non-FLS clouds present were classified as "multi-

215 layer" (FLS beneath non-FLS clouds), while others remained "FLS". Worth mentioning that as the non-FLS cloud screening

9

procedure explained above uses the SEVIRI $\rho_{0.6}$, $\rho_{1.6}$ data, its ~~application~~applicability is limited to daytime (i.e., solar zenith angles ≤ 80°). For this reason, despite the availability of both the SEVIRI and METAR data over day and night, the FLS labels derived here are limited to the daytime only. It should also be noted that, ~~although~~despite overall reliability of the procedure applied here for detection of "non-FLS-cloud" contaminated cases ~~is rather legit, there times that it,~~ the method sometimes

220   fails to detect ~~them. As a result of this failure, some of the labels may have been mistakenly modified. Specifically, some~~non-FLS clouds, leading to occasional misclassifications (e.g., multi-layer ~~and~~or non-FLS-cloud ~~conditions may have been mistakenly~~cases labelled as FLS ~~and~~or clear-sky ~~(and vice versa), respectively.).~~ Nevertheless, initial tests ~~for fitting~~of a ~~ML~~machine learning model ~~over the data~~ showed that ~~application of the abovementioned~~ using this procedure ~~for detection of non FLS clouds is very~~ is essential for ~~optimizing the model's performance in identification of the FLS conditions.~~ making

225   the ground observations compatible with what is seen from space.

~~In~~ 3.2 FLS flag quality assessment

The quality of the modified FLS labels in terms of sky condition homogeneity was assessed by comparing the labels corresponding to each timestamp at each station with that of its previous and next timestamps at the same station. Particularly, for each three consecutive data points at the same location the middle data point was set to:

230
- "no confidence", if the time difference between the first and third data points was greater than 1hr, or the FLS label for neither first nor third data point were the same as the middle one.
- "semi-confident", if the FLS label for one of the first or third data points was the same as that of the middle one.
- "confident", if the FLS label for both the first and third data points was the same as that of the middle one.

This quality control procedure was considered to identify data-points with homogeneous sky condition and to minimize the

235   uncertainties associated with spatio-temporal matching of the SEVIRI data with the ground station data, the coordinate system used for geolocation of SEVIRI pixels, and coordinates of the ground stations. The SEVIRI pixels have a spatial resolution of about 3 km at nadir which results in a resolution between 4 to 8 km over Europe. Plus, there is up to 0.3 km of uncertainty associated with the procedure applied by EUMETSAT for georeferencing SEVIRI images. Additionally, the satellite is not exactly stationary on the geostationary ring and its true position varies slightly with time because all satellites are drifting from

240   their nominal position. On the other hand, the ground stations are not exactly located at the center of the SEVIRI pixels, and some are indeed on the borders of the pixels. Also, there may exist occasions where the METAR location within the pixel has a different sky cover compared to the majority of the pixel area. This can be the case with pixels contaminated by the edges of non-FLS clouds or cloud layers which are forming, but are not yet fully developed (cf. ~~step, the~~Jahani et al., 2020, 2022; Koren et al., 2007). The sky conditions for the data points surviving this quality control procedure are assumed to be homogeneous

245   at subpixel level.

3.3 Training and testing datasets

The entire data was split into five datasets, namely, "~~train~~training", "$test_1$", "$test_2$", "$test_3$" and "$test_4$". Table 1 ~~provides a summary about~~ summarizes the characteristics of these datasets and ~~Fig.~~Figure 1 shows the location of the stations included in each of them. The ~~train~~training dataset was used for training the ML algorithm. $test_1$ dataset was intended to evaluate the performance of the trained model over locations seen by the model during training, but at time spans beyond ~~that of the data seen by the~~those used for model ~~during~~ training. The datasets $test_2$, $test_3$ and $test_4$ were intended for quantifying the accuracy of the trained model over locations which were never seen by the model during the whole study period. The sampling for the data split was done based on the time frame of the observations and the FLS occurrence regimes identified according to FLS flags described in Section 2.4.

To split the data~~ to the five datasets~~, the annual frequency of FLS occurrence at each station was first determined by calculating the ratio of the daytime FLS positive labels to all valid labels in METAR per winter year (i.e., 2016-2017, 2017-2018, …). In the second step, the annual ratios were averaged over the study period to obtain the mean annual frequency of FLS occurrence at each station ($\bar{f}$, range of the values obtained: 0.~~00~~0.-12~~)~~.0%). In the third step, the stations were grouped into 23 bins based on their $\bar{f}$ values (bin widths: 0.~~005)~~.5%). The entire data corresponding to the stations falling in the first two $\bar{f}$ bins (i.e., $\bar{f}$<~~0.01)~~1%) were considered as the $test_4$ dataset (59 stations). This dataset was intended to evaluate the ~~algorithms'~~algorithm's performance at ~~location~~locations where FLS rarely occurs. In the fourth step, from each of the 21 remaining $\bar{f}$ bins, one random station per bin was selected to construct the $test_2$ and $test_3$ datasets. Among all the datapoints corresponding to these 21 stations, those ~~covering~~that cover the winters (September to May) of 2018-2019 and 2021-2022 comprise the $test_3$ dataset, and the remaining ones comprise the $test_2$ dataset. These two datasets are considered for validating the algorithms at locations other than those used for training the ML model. As can be understood, the difference between the two is the time span covered by them. In particular, the time spans covered by ~~the~~ dataset $test_2$ are the same as those of the dataset used for training, and $test_3$ dataset covers time spans beyond those covered by the ~~train~~training dataset. Lastly, the $test_1$ and ~~train~~training datasets were then constructed by splitting the data corresponding to the 276 stations which were not allocated to $test_2$, $test_3$ or $test_4$. Specifically, the data points corresponding to the winters (September to May) of 2018-2019 and 2021-2022 comprised $test_1$ dataset, and those corresponding to the winters of 2016-2017, 2017-2018, 2019-2020 and 2020-2021 comprise the ~~train~~training dataset. As can be inferred, the data points corresponding to the stations with $\bar{f}$ less than ~~0.01~~1% were not included in the ~~train~~training dataset. This data was excluded from the ~~train~~training dataset to decrease the imbalance between the FLS positive and negative cases. That is because the initial tests of the algorithm indicated that the data corresponding to the stations with $\bar{f}$ less than ~~0.01~~1% in the ~~train~~training dataset vastly increases the imbalance between FLS positive and negative cases, which ~~lead~~leads to a decrease in the algorithm's skill for detecting the FLS cases. ~~This~~These data ~~was~~points were, however, included in the analysis as ~~test₃~~test₄ dataset to evaluate the algorithm's performance at places that FLS rarely occurs.

~~Afterwards, the quality of the modified FLS labels was assessed and the case~~Next, the cases of "no confidence" and "semi-confident" FLS were removed from the ~~four datasets. This was done by comparing the labels corresponding to each timestamp~~

at each station with that of its previous and next timestamps at the same station. Particularly, three consecutive data points at the same location were chosen each time. If the time difference between the first and third data points was greater than 1hr, or the FLS label for neither first nor third data point were the same the middle one, the quality flag for the middle data point was set to "no confidence". If the FLS label for one of the first or third data points was the same as that of the middle one, then the quality flag for the middle data point was set to "semi-confident". Lastly, if the FLS label for both the first and third data points was the same as that of the middle one, then the quality flag for the middle data point was set to "confident". This quality control procedure was considered to select the data points with homogeneous sky condition and to cope with the uncertainties associated with spatio-temporal matching of the SEVIRI data with the ground station data, the coordinate system used for geolocation of SEVIRI pixels, and coordinates of the ground stations. The SEVIRI pixels have a spatial resolution of about 3km at nadir which results in a resolution between 4 to 8km over Europe. Plus, there is up to 0.3km of uncertainty associated with the procedure applied by EUMETSAT for georeferencing SEVIRI images. Additionally, the satellite is not exactly stationary on the geostationary ring and its true position varies slightly with time because all the satellites are drifting from their nominal position. On the other hand, the ground stations are not exactly located at the centre of the SEVIRI pixels, and some are indeed on the borders of the pixels. Also, there may exist occasions where the METAR location within the pixel has a different sky cover compared to the majority of the pixel area. This can be the case with pixels contaminated by the edges of non-FLS clouds or cloud layers which are forming, but are not yet fully developed (cf. Jahani et al., 2020, 2022; Koren et al., 2007). The sky conditions for the data points surviving this quality control procedure are assumed to be homogeneous at the subpixel level.

Next, the case five datasets and the cases of "multi-layer" conditions were relabelledrelabeled as "non-FLS-cloud" for the test$_1$, test$_2$, test$_3$, and test$_4$ datasets but were removed completely from the traintraining dataset. They were removed from the traintraining dataset to have excluded theeliminate cases that can potentially be ambiguous and thus havecould introduce ambiguity, ensuring the ML model is trained on a dataset which containsdata with a clear discriminationdistinction between "non-FLS-cloud" and the two other classes (i.e., "clear-sky" and "FLS"). The METAR FLS labels generated in this way (hereafter referred to as "MFL)") serve as the ground truth and will be used for the model development and validation purposes. A summary of the data included in the final four datasets is given in Table 1. A schematic description of the process followed in this section for creation of the MFL included all the five datasets is provided in Fig.Figure A1. As this table shows, the datasets traintraining, test$_1$, test$_2$, and test$_3$ contained an overall number of 1168921, 644804, 142641, and 588034 data points, respectively. This table also shows that the number of non-FLS cases (i.e., clear-sky and non-FLS-cloud classedclasses combined) is substantially higher than that of the FLS cases. Nevertheless, the factionfraction of FLS cases is in the same range for the datasets traintraining (3.8 %), test$_1$ (3.3 %), test$_2$ (4.7 %), and test$_3$ (4.4 %) whereas that of test$_4$test$_4$ (0.2 %) is considerably lower than that of the other three datasets. It should be noted that the FLS labels prior to application of quality flags were used for the data split, because the goal was to sample data based on different FLS regimes. Whereas the quality checks were mainly applied to flag data points that are likely to represent homogeneous sky conditions,

Table 1. Summary of the data contained in the "~~train~~training", "test$_1$", "test$_2$", and "test$_3$" datasets. The values given in this table are based on the final datasets (i.e., they are derived based confident FLS labels).

Dataset	Time span	Stations	Total data points	Label frequency in the entire dataset (%)		
				clear-sky	FLS	non-FLS-cloud
~~train~~training	2016-2017 2017-2018 2019-2020 2020-2021	276	1168921	35.6	3.8	60.6
test$_1$	2018-2019 2021-2022	276	644804	33.4	3.3	63.3
test$_2$	2016-2017 2017-2018 2019-2020 2020-2021	21	95818	32.3	4.7	63.0
test$_3$	2018-2019 2021-2022	21	46823	33.9	4.4	61.7
test$_4$	2016-2022	59	588034	39.1	0.2	60.7

320

~~2.5~~3.4 Machine learning algorithm

In the present study, ~~a~~an XGBoost (gradient boosted trees) model was developed for FLS detection over Europe based on SEVIRI observations in the LIR (Long-wave InfraRed) spectral region. XGBoost is a well-tested supervised ML (machine

learning) technique which has been successfully applied to many regression and classification problems. It extracts the nonlinear relationships between sets of input variables/features and a target output variable through constructing an ensemble of sequentially built regression trees (also referred to as "weak learners)") to the data. The regression trees are added one at a time to the ensemble to correct for the deficiencies in the previous modelregression tree and minimizingto minimize a specified loss function. All these trees together construct a powerful statistical model referred here to as "XGBoost.". For this model, the prediction is performed by summing over all the regression trees. Once the model is trained, the role of each input feature in constructing the boosted decision trees within the model is indicated based on a metric referred to as "feature importance.". The more an input feature is used to make key decisions with decision trees, the higher its importance. For more information about XGBoost please refer to (Friedman, 2001; Mitchell & Frank, 2017; Natekin & Knoll, 2013).Mitchell and Frank (2017), Friedman (2001), and Natekin and Knoll (2013). The open source XGBoost python implementation (https://xgboost.readthedocs.io/en/stable/index.html, last access: 28.03.2023) was used in the present study.

The XGBoost model was trained to predict the labels "FLS", "non-FLS-cloud", and "cloud-free" based on a set of input variables generated from the channel and channel combinations $BT_{12.0}$, $BT_{8.7}$ - $BT_{12.0}$, $BT_{10.8}$ - $BT_{12.0}$, and $BT_{12.0}$ - $BT_{13.4}$ plus the standard deviation of each of these variables in a spatial window sized 3x3 pixels with the central pixel being the target pixel.

The pixel values of the mentioned variables contain information about the cloud presence, cloud top height, phase, particle radius for the area falling within the limits of the target pixel and their standard deviationsand the particle radius for the area falling within the limits of the target pixel. Specifically, the SEVIRI channels centered at 8.7, 10.8, and 12.0 μm wavelengths fall within the atmospheric window region (where the absorption by the atmospheric gases is minimal) and the one at 13.4 μm is in a CO_2 absorption region. The $BT_{8.7}$ - $BT_{12.0}$ and $BT_{10.8}$ - $BT_{12.0}$ provide data on the spectral dependency of the emissivity of the surface/cloud covering the scanned scene. This data gives information about the size and thermodynamic phase of the particles at the cloud top (Strabala et al., 1994) in case of cloudy scenes, and about surface properties for the clear-sky scenes (e.g. Petitcolin and Vermote, 2002; Andersen and Cermak, 2018). $BT_{12.0}$ - $BT_{13.4}$ is linked to the absorption depth of CO_2, which can be used as a proxy for determining the depth of the atmospheric column. This information can be interpreted as the height of the emitting body (surface/cloud). $BT_{12.0}$ is a proxy for the temperature of the emitting body, which can play a role in determination of its height and phase. The standard deviations of the channel combinations mentioned above summarize the heterogeneity of this information over the 3x3 pixel area around the target pixel. The standard deviations were considered because the different land and cloud types tend to show different degrees of spectral and spatial heterogeneity.

The hyperparameters of the model were tuned to optimize the model's performance and avoid overfitting. This was done based on the statistical indicators explained in Appendix B. To this aim, a grid-search was performed to find the optimum values of the XGBoost hyper parameters learning rate (0.3), maximum depth (5), minimum child weight (1), number of regression trees (100), alpha (0), and lambda (1). The XGBoost model trained this way was then applied to the entire SEVIRI scenes acquired in the present study (see Sect. 2.1), including the SEVIRI pixels over water.

Formatted: Centered

3.5 Feature selection

The set of input variables mentioned ~~above~~in Section 3.4 were selected by analysing the spectral SEVIRI LIR data and the corresponding ~~the~~ MFLs included in the "~~train~~training" dataset with the objective of creating the simplest model possible that can capture general differences between FLS and the two other classes (i.e., non-FLS-cloud and cloud-free). Here, the simplest model is defined as an accurate model (according to Eqs. ~~(1-7)~~B1-B7) capable of detecting FLS based on minimal spectral and spatial input data. To select the most relevant input features for discriminating FLS from the two other classes (i.e., those that reduce the error the most), we tested the data corresponding to the LIR channels ~~BT_8~~centered at 8.7, ~~BT_9~~9.7, ~~BT_{10}~~10.8, ~~BT_{12}~~12.0, and ~~BT_{13}~~13.4 μm ~~wavelengths~~ along with all the 10 possible combinations which can be derived from subtracting them from one another ~~were tested~~. This was done by applying the feature selection technique referred to as "backwards elimination". To this aim, ~~a~~an XGBoost model was initially trained to predict FLS labels using all the input features. The features were then iteratively removed (one feature was dropped per iteration) based on their low gains in fitting (feature importance), leading to a series of models, ~~totalling 15. The accuracy of these 15 models in detection of the FLS was evaluated based on Eqs.(1-7) given in Sect. 2.6.~~totalling 15. The simplest combination of input features was then selected by comparing the accuracy of the models 2 to 15 with that of the first model (the most complex one was considered as the reference). This revealed that the accuracy drops gradually as features decrease, with a significant drop when a key feature is removed. The model just before this drop signifies the minimal essential feature set. ~~In this way, the variables $BT_{12.0}$, $BT_{8.7} - BT_{12.0}$, $BT_{10.8} - BT_{12.0}$, and $BT_{12.0} - BT_{13.4}$ were chosen as the most essential inputs for the XGBoost model.~~ Additional tests also indicated that including the standard deviations of these variables in a 3x3 pixel area around the target pixel helps ~~increasing~~to increase the accuracy of the model and for this reason~~,~~ they were considered as input features to the model.

~~The hyperparameters of the model were tuned to optimize the model's performance and avoid overfitting. This was done on the basis of the statistical indicators explained in Sect. 2.6. To this aim, a grid-search was performed to find the optimum values of the XGBoost hyper-parameters learning rate (0.3), maximum depth (5), minimum child weight (1), number of regression trees (100), alpha (0), and lambda (1). The XGBoost model trained this way was then applied to the entire SEVIRI scenes acquired in the present study (see Sect. 2.1), including the SEVIRI pixels over water.~~ The metrics used for selection of the hyperparameters are presented in Sect. 2.6.

~~2~~3.6 Validation

The skills of the newly proposed ML and the established SOFOS FLS detection algorithms were quantified and compared by validating them versus the MFLs corresponding to the "~~train~~training", "$test_1$" and "$test_2$" datasets. The validation for each dataset was performed by calculating the statistical indicators *Probability of Detection* (*POD*), *False Alarm Ratio* (*FAR*), *Probability of False Detection (PFD), Critical Success Index (CSI), Accuracy (ACC), Bias Score (BS),* and *distance from optimal point (d)* as ~~follows:~~

~~$$POD = N_H / (N_H + N_M) \qquad (1)$$~~

15

$$FAR = N_F / (N_H + N_F) \qquad (2)$$

$$PFD = N_N / (N_F + N_N) \qquad (3)$$

$$CSI = N_H / (N_H + N_M + N_F) \qquad (4)$$

$$ACC = (N_H + N_N) / (N_H + N_N + N_F + N_M) \qquad (5)$$

$$BS = (N_H + N_F) / (N_H + N_M) \qquad (6)$$

$$d = ((POD\text{-}1)^2 + FAR^2)^{0.5} \qquad (7)$$

where N_H, N_M, N_F, and N_N are the number of *hits*, *misses*, *false alarms*, and *true negatives*, respectively. A *hit* (*true negative*) refers to a condition which is classified as FLS (non-FLS; clear-sky or non-FLS cloud) by both the algorithm and MFLs. A FLS condition (as indicated by MFLs) which is identified as non-FLS by the product is referred to as a *miss*, and the opposite is referred to as a *false alarm*. It should be noted that one of the four cases can be true for a data point only indicated in Appendix B. These statistical indicators. *POD* quantifies the skill of the method in correctly identifying the FLS cases. *FAR* indicates the portion of false alarms among all the cases classified as FLS by the algorithm. *PFD* highlights the portion of the non-FLS cases which have been correctly classified as non-FLS by the algorithm. *CSI* is a metric indicating the overall correctness of the FLS classification. *ACC* shows the portion of the cases which have been correctly identified as FLS and non-FLS. The metrics *POD*, *FAR*, *PFD*, *CSI,* and *ACC* vary between 0 and 1. An ideal detection algorithm should have a *POD, PFD, CSI,* and *ACC* equal to 1, and *FAR* equal to 0. *BS* reflects the overall bias of the product. *BS* varies in between 0 and $+\infty$, with the optimal value being 1. The values of *BS* greater and smaller than 1 reflect over- and under-estimation of the FLS class, respectively. As can be inferred from Eq. (6), *d* is a metric obtained by combining the statistical indicators *POD* and *FAR* and compares the performance of the algorithm with the ideal algorithm (*FAR: 0, POD: 1*). In other words, it indicates how distant the performance of the FLS detection algorithm is in comparison with that of the best algorithm which can ideally exist. *d* varies between 0 and $\sqrt{2}$, with 0 being the ideal value.

The statistical indicators described above were calculated using the entire data points included in each dataset to evaluate and compare both algorithms' overall performance over the train training and four test datasets.

3 Validation results

4 Results and discussion

Figure 2 summarizes the results obtained from validating the ML and SOFOS FLS algorithms against the MFLs corresponding to the "train training", "test$_1$", "test$_2$", "test$_3$" and "test$_4$" datasets. The statistical indicators given in this figure were calculated using all the data points present in the five datasets (see Table 1 for more information about the exact number of data points included in each dataset is provided in Table 1). Thus,), therefore they can be interpreted as the overall performance of the algorithms over all the regions and time spans covered by each dataset. Validation of the ML product versus the MFLs included in the train training dataset revealed an overall classification accuracy of 0.60 and 0.98 in terms of *CSI* and *ACC* metrics for

16

the algorithm, respectively. The algorithm was able to correctly label about 80% of the FLS and 99% of the non-FLS (clear-sky or non-FLS-cloud) situations included in training dataset (POD: 0.80 and PFD: 0.99). The FAR score obtained by the ML product for the same dataset was 0.30, which resulted in a d of 0.36. The FAR of 0.30 indicates that 30% of the situations labelled as FLS by the ML product were reported as non-FLS by the ground based MFLs. Because of these false alarms the FLS occurrence frequency computed for the training dataset based on the ML product is overestimated by about 14% compared to the determination made by the MFLs (BS: 1.14). Overall, these numbers show that the ML algorithm proposed here was capable of detecting the majority of the FLS situations over the locations and time spans included in the training dataset. Considering that the algorithm was trained using these exact data points, it can be inferred that the algorithm was able to capture the subtle yet discernible distinctions between FLS and non-FLS situations (in the LIR spectral region) at locations and time spans covered by the training dataset. This is further reinforced by comparing these error metrics with those calculated for the state-of-the-art daytime SOFOS algorithm for validation versus the same dataset. the CSI, ACC, and PFD scores obtained by SOFOS were 0.59, 0.98, and 0.98 respectively, which are close to what was obtained by the ML algorithm. On the other hand, SOFOS showed a higher POD (0.92) compared to the ML algorithm, which was achieved at the cost of a higher FAR (0.38), leading to larger d and BS (0.38 and 1.47, respectively). Specifically, the number of data points labelled as FLS by SOFOS was 14027 (29%) greater than what was reported as FLS by the ML algorithm. Only about one third of these data points, however, were correct calls and the rest were false alarms. In fact, all of these false alarms must have been identified as clear-sky by the MFLs. That is because the criteria considered in the MFLs for screening out the non-FLS clouds is the same as the one used by SOFOS. Thus, the case of non-FLS-cloud class included in the MFLs matches well with that of SOFOS and the validation approach presented here essentially evaluates the skill of SOFOS in discriminating the FLS and clear-sky situations from each other. One implication of these differences can be the fact that the ML algorithm considers a stricter criterion compared to SOFOS for classifying a situation as FLS, resulting in a more confident FLS identification. On the other hand, these misclassifications could also correspond to the cases of snow-covered land under clear sky conditions. Nonetheless, heterogeneity of topography at a subpixel scale could have a strong impact on this evaluation. This is particularly important here due to the coarse resolution of the SEVIRI pixels over Europe. Subpixel heterogeneity of topography can be problematic for validating these products as the sky condition in the area covered by the SEVIRI pixel are not well represented by station measurements. Specifically, there may exist situations where the station measurements indicate a clear-sky condition, whereas the majority of the SEVIRI pixel area is covered by FLS (and vice versa). However, understanding the influence of topographical heterogeneity at a subpixel scale on the FAR and BS scores can be quite challenging, and is out of the scope of the current study.
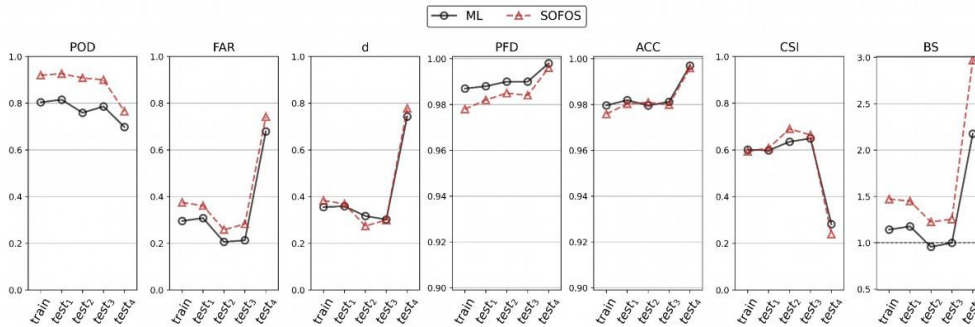
Figure 2. Validation results of the ML (black ~~line/circle~~circles) and SOFOS FLS detection algorithms (red ~~line/triangle~~triangles) versus the modified METAR FLS Labels (MFLs) for the "~~train~~training", "test₁", "test₂", "test₃", and "test₄" datasets.

Based on the preceding discussion, it can be inferred that the ML algorithm is competent and appropriate for distinguishing between FLS and non-FLS situations. This accomplishment aligns with the initial hypothesis of this study, which states that spectral LIR data can be used to differentiate FLS from cloud-free land and non-FLS clouds with comparable accuracy to an existing state-of-the-art daytime FLS detection ~~algorithms. To ascertain the applicability and generalization of the newly proposed approach to locations and time periods not used in the training, the performance of the ML~~ algorithm ~~was rigorously assessed using the test₁, test₂, and test₃ datasets. To gauge its effectiveness, the algorithm's results were compared with those obtained for SOFOS using the same datasets (Fig.~~. The information provided in Figure 2~~). These results~~ overall ~~suggest~~suggests that the ML algorithm applicability expands beyond locations and time periods covered by the ~~train~~training dataset. ~~For example,~~Specifically, the results obtained from validation versus the test₁ dataset ~~includes data points from the same stations as the training dataset, but it covers~~confirm the technique's applicability to time periods that are not included in the training dataset. The CSI, ACC, and PFD scores obtained by the ML model for validation versus the test₁ dataset were respectively equal to 0.60, 0.98, and 0.99, which are the same as those reported for the ~~train~~training dataset. Nonetheless, ~~the~~ POD and FAR values derived from validating the ML algorithm with test₁ dataset were slightly higher than those obtained through ~~validating it~~validation with the ~~train~~training dataset (0.82 and 0.31, respectively). Consequently, this results in a slightly increased BS (1.18), while the value of d remains the same (0.36). ~~The test₂ dataset evaluates the algorithm's FLS detection capability at locations outside the train dataset but within the same time spans. On the other hand, the test₃ dataset evaluates the algorithm's performance at locations and time spans that it has never encountered during training. For the test₂ dataset, the ML algorithm achieved a CSI score of 0.64, an ACC score of 0.98, and a PFD score of 0.99. Additionally, the algorithm's POD was 0.76, with a FAR of approximately 0.21. This resulted in a d of 0.32 and a BS of 0.96. Similarly, for the test₃ dataset, the ML algorithm achieved a CSI score of 0.65, an ACC score of 0.98, and a PFD score of 0.99. The algorithm's POD was 0.79, with a FAR of around 0.21. This resulted in a d of 0.30 and a BS of 1.00.~~ As it can be inferred from ~~Fig.~~Figure 2, ~~these~~

~~numbers~~ the statistics obtained by the ML algorithm over test$_2$, and test$_3$ compare very well with those obtained by SOFOS ~~for the three test datasets.~~. In particular, *ACC*, *CSI* and *PFD* were merely the same for both algorithms over the ~~three~~two test datasets. On the other hand, the *POD* and *FAR* values obtained by SOFOS were both higher than those obtained by the ML algorithm which ~~result~~results in a similar *d* but higher *BS* scores. ~~Lastly, the ML algorithm was validated~~Validation with test$_2$ dataset confirms the algorithm's FLS detection capability at locations outside the training dataset but within the same time spans. The results obtained from the test$_3$ dataset prove the algorithm's effectiveness at locations and time periods not encountered during training. Validation versus the test$_4$ dataset ~~to evaluate its performance at locations where FLS rarely occurs. This~~ is particularly important here because none of the two algorithms ~~have been~~were originally designed for ~~such~~ regions included in the dataset. Nonetheless, results obtained from this validation should be interpreted with care due to the low number of FLS cases (as identified by MFLs) included in this dataset. In particular, the test$_4$ dataset only includes nearly 0.2% FLS cases and as a result, even one random misclassification can have a strong ~~effect~~impact on the error metrics *FAR*, *d*, *CSI* and *BS*. For this reason, the evaluation of the algorithm in this region is done solely based on the metrics *POD*, *PFD* and *ACC*. As can be seen from ~~Fig.~~Figure 2, validation of the ML (SOFOS) algorithm with ~~the~~ test$_4$ ~~gave~~yielded high values of *POD*, *PFD*, and *ACC*, ~~being~~ equal to 0.70 (0.76), ~1.0 (~1.0), and ~1.0 (~1.0), respectively. These numbers prove that the ML algorithm developed in the present study is applicable to regions where FLS rarely occurs.

Overall, the error metrics given above (and shown ~~Fig.~~Figure 2) show that the ML FLS detection algorithm developed here is suited for application over Europe. In particular, the algorithm features an accuracy very similar to that of the the-state-of-the-art daytime SOFOS algorithm, but has the advantage of operating based on SEVIRI LIR bands, which allows ~~it to be applied~~its application over the 24H of the diurnal cycle. Worth mentioning that the error metrics calculated here for SOFOS are somewhat different compared with those reported in ~~Cermak & Bendix (2008)~~Cermak & Bendix (2008) and Egli et al. (2018) for this algorithm, although the METAR data was used for validation purposes in the two studies. Specifically, the *POD*, *FAR*, and *CSI*, as reported by ~~Cermak & Bendix (2008)~~Cermak & Bendix (2008) for SOFOS, ranged from 0.76 to 0.83, 0.~~06~~02 to 0.~~02~~06, and 0.73 to 0.82, respectively. In the study by Egli et al. (2018), the reported values of *POD* and *FAR* for SOFOS were 0.52 and 0.66, respectively. There are several reasons contributing to these differences. One reason can be the additional processing steps involved in the present study for the generation of MFLs compared ~~with those applied in~~to the other two studies: applying the quality flags and marking the non-FLS-~~cloud~~clouds contaminates pixels. The difference in the location of the stations selected and the number of data points utilized for the validation highly impact the validation results. Additionally, as these error metrics are calculated as relative statistics, the absolute number of FLS/non-FLS cases included in the datasets used for validation can make a big difference in the results obtained. This is particularly important here because they are calculated relative to a small subset of the data: the FLS-positive cases (as identified by the truth or predicted product) which are inherently low in number. This is especially relevant in Europe, where about 30% of FLS events are obscured by other clouds (Cermak, 2018). As a result of the relatively small denominator, they can show a relatively high degree of sensitivity to a few misclassifications. In addition, it should be noted that they do not provide a global image about the overall classification accuracy of the product, as they do not account for the "*true negative*" instances, which are very large in number for FLS. For

19

510 these reasons, although the metrics *POD*, *FAR*, *CIS* and *BS* provide essential and detailed information about the product's performance, they need to be interpreted with care. To account for these two matters the error metrics *ACC* and *PFD* were introduced. As the denominator of these metrics is rather large and they take the "*true negative*" instances into consideration, they are expected to be better suited for showing the product's overall performance over the whole dataset.

4Figure 3 illustrates the calibrated SEVIRI Level 1.5 products over the study region on 02 March 2021—a representative day
515 with presence of persistent FLS in Europe—at three distinct scan times (13:00, 16:30, and 20:00 UTC), along with the corresponding outputs generated by the ML FLS detection algorithm developed in this study. In this figure, the panels in the left column (a, d, and g) show $\rho_{0.6}$. Panels in the middle column (b, e, and h) show a false-color RGB image constructed based on the SEVIRI LIR data, with the red, green, and blue channels being $BT_{12.0} - BT_{13.4}$, $BT_{8.7} - BT_{12.0}$, and $BT_{10.8} - BT_{12.0}$, respectively. Panels in the right column (c, f, and i) illustrate the classifications produced by the ML FLS detection algorithm,
520 with the classification categories including clear-sky (khaki), FLS (red), and non-FLS-cloud (blue). In each panel, solar zenith angle values are represented by colored contour lines. The data presented in this figure highlights the consistency of the ML FLS detection algorithm across different conditions: daytime (top row), the day-night transition (middle row), and nighttime (bottom row), as well as over various surface types, including water, land, and land-water transition points. Supplement animation (S1) shows the full sequence of the false color RGB satellite images and the corresponding classification maps over
525 the 24H cycle of 02 March 2021.

The presence of a widespread FLS event around 55° N, with partial contamination by non-FLS clouds can be observed from Figure 3(a). Additionally, two smaller regions are visible: one near 50° N, 15° E, and another near 50° N, 10° W. These areas are characterized by a smooth texture and high reflectivity. In Figure 3(b), the FLS-covered regions are distinguishable by their smooth texture and dark red coloration, while the non-FLS clouds appear in green with greater spatial variability
530 compared to FLS regions. Figure 3(c) demonstrates the algorithm's effectiveness in identifying both FLS-covered regions and the non-FLS clouds passing over these areas. Notably, the algorithm's performance remains robust, with no sudden changes or misclassifications observed, even when applied to water, land, or land-water transition points. Apart from slight changes in the coverage, FLS persists over the mentioned regions until the end of that day (see S1 for more information), which can be traced in Figures 3(e) and 3(h). As can be seen in Figures 3(f) and 3(i), the algorithm continues to accordingly and consistently
535 identify the FLS covered regions over land and water during the day-night transition time and at night. Here again, the algorithm's performance remains robust, with no sudden or solar zenith angle dependent changes/misclassifications observed. However, it is worth mentioning that for the three scans shown here the algorithm categorizes the area near 47° N, 10° E (the Alps), which appears to be snow-covered, as non-FLS-cloud contaminated. This is because, as Figures 3(b, e and h) show, snow-covered land and non-FLS clouds exhibit similar characteristics in the LIR range.

Formatted: Centered
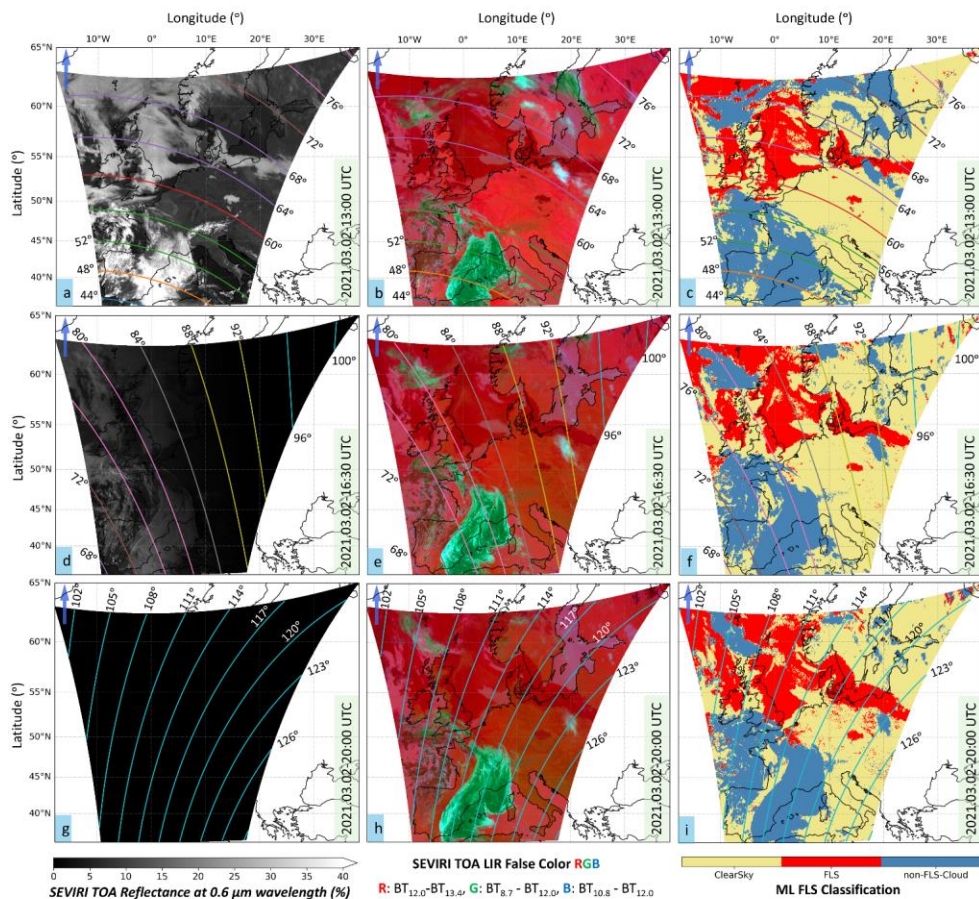
Figure 3. Comparison between calibrated SEVIRI level 1.5 products over the study region on 02 March 2021 at three different scan times (13:00, 16:30, and 20:00 UTC) and the corresponding outputs yielded from the ML FLS detection algorithm developed in the present study. Pannels in the left (a, d, and g), middle (b, e, and h), and right columns (c, f, and i) respectively represent $\rho_{0.6}$ (%), false color RGB composite based on $BT_{8.7}$, $BT_{12.0}$, and $BT_{13.4}$, and the classifications produced by the ML FLS detection algorithm. FLS classification categories include clear-sky (khaki), FLS (red), and non-FLS-cloud (blue). Overlayed colored contour lines represent solar zenith angle (degrees) for reference. Note: solar zenith angles greater than 95° are represented in turquoise color. Supplement animation (S1) shows the full sequence of the false color RGB satellite images and the corresponding classification maps over the 24H cycle of 02 March 2021.

Formatted: Centered

21

5 ~~Summary,~~ Conclusions and outlook

The main objective of the present study was to develop a diurnally stable algorithm for detection of FLS over Europe based on ~~the observation of~~observations from the SEVIRI instrument onboard MSG satellites with an accuracy comparable with that of the state-of-the-art daytime FLS detection ~~algorithms~~algorithm. The algorithm proposed here consists of a gradient boosting (XGBoost) machine learning model ~~(XGBoost)~~ that is trained to classify each SEVIRI pixel as "clear-sky", "FLS", or "non-FLS-cloud" based on ~~the~~ SEVIRI observations in the LIR bands. Specifically, the classification is performed based on pixel values of $BT_{12.0}$, $BT_{8.7} - BT_{12.0}$, $BT_{10.8} - BT_{12.0}$, and $BT_{12.0} - BT_{13.4}$ plus the standard deviation of each of these variables in a spatial window sized 3x3 pixels with the central pixel being the target pixel.

Six years of daytime ground-based observations from Meteorological Aviation Routine Weather Reports (METAR) at 356 European locations ~~was~~were utilized to generate ground truth FLS labels for training and evaluating the algorithm. Lastly, a comparison between the accuracies of the newly proposed ML and ~~a~~the state-of-the-art daytime FLS detection algorithm (SOFOS) was performed to address the objective of the study.

The results obtained from validating the FLS products against ~~the~~ training and the four test datasets revealed that the ML FLS detection algorithm proposed here is capable of discriminating ~~the~~ FLS from other sky conditions, and ~~that~~ its applicability in the study region (i.e., Europe) extends beyond the particular locations and time spans covered by the datapoints used for training the algorithm. Specifically, the ML algorithm features an accuracy very close to that of SOFOS over all ~~the~~ five datasets. The main difference between the two is in the POD, FAR, and BS ~~achieved by them~~metrics: SOFOS features a slightly higher POD compared to the ML algorithm. On the other hand, it suffers from a higher FAR and BS compared to the ML algorithm. One ~~implication of~~could argue that these differences ~~can be~~occur due to the fact that the ML algorithm considers a more ~~restrict~~restricted criteria for classifying a situation as FLS, resulting in~~ a~~ a more confident FLS ~~class.~~classification. Another advantage that the ML algorithm has over SOFOS is that it operates solely based on ~~the~~ SEVIRI channels in the LIR spectral region, which allows it to be applicable over the 24H of the ~~diurnal~~day cycle. In addition, the ML FLS detection algorithm presented here is efficient in terms of computation time. This makes the algorithm very suitable for operational purposes such as monitoring, nowcasting, and forecasting of FLS as well as reprocessing the historical SEVIRI data. Furthermore, as the algorithm is the first of its kind that is a single algorithm applicable over day and night over Europe, it can potentially provide new insights into the FLS life cycle over Europe and help enhancing the performance of existing FLS forecast products. This will be of particular use in the development of short-term forecasts of FLS dissipation for applications such as photovoltaic power forecasting.

Nonetheless, it should be noted that there are limitations associated with the validation procedure performed here: ~~Although~~although the algorithm presented here classifies the ~~states~~state of the sky into the three ~~classes~~categories "clear-sky~~,~~", "FLS" and "non-FLS-cloud~~.~~", the validation procedure presented here only evaluates its skill in differentiating the FLS situations from ~~the~~ "clear-sky" and "non-FLS-cloud~~.~~". Its skill in discriminating between clear-sky and non-FLS-cloud situations ~~yet~~ remains ~~to be~~ unvalidated due to limited information obtained from METAR ~~observation~~observations. Further,
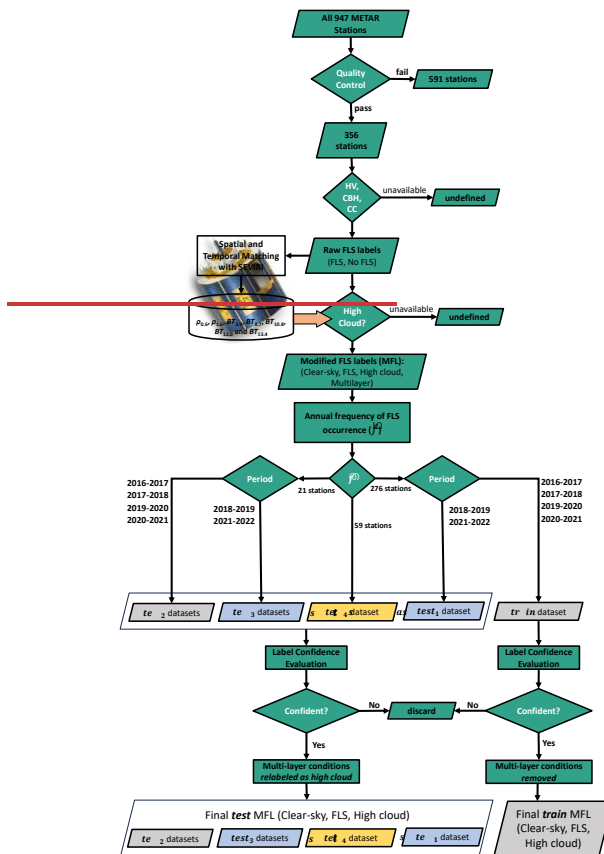
22

although the ML algorithm presented here operates based on SEVIRI LIR bands, we ~~have~~were not ~~been~~ able to provide a quantitative evaluation of its accuracy over nighttime, as the procedure applied here for the identification of the non-FLS-clouds falling withing SEVIRI's FOV consisted of thresholding the SEVIRI channels falling within the limits of the solar spectrum. Additionally, it should be noted that all ~~the~~ datapoints used in the present study for algorithm ~~evaluations~~evaluation are located over land and limited to the European region. For this reason, the algorithm's applicability over water and ~~at~~in other ~~regions is~~areas was not quantitatively validated. Nevertheless, the diurnal stability and applicability of the algorithm over water as well as its ability to discriminate non-FLS-clouds from clear-sky ~~situation~~situations were confirmed through visual inspection of several sequences of satellite images and the corresponding ~~resulting~~ classification maps. See the supplement animation (S1) for more information. In this animation, the left~~-hand~~ panel shows a false-color RGB image constructed based on the calibrated SEVIRI ~~raw channel~~level 1.5 data with the red, green, and blue channels being $BT_{12.0}$ - $BT_{13.4}$, $BT_{8.7}$ - $BT_{12.0}$, and $BT_{10.8}$ - $BT_{12.0}$, respectively. In this panel, the green color represents the high clouds, and the light and dark red colors represent ~~the~~ clear-sky and FLS, respectively. The right~~-hand~~ panel ~~of this animation also~~ shows the outputs of the ML FLS detection algorithm developed in the present study.

In addition to the limitations discussed above, there are ~~also some degrees of uncertainty involved with~~ other limiting factors contributing to the validation ~~process~~ performed here, which originate from the ~~spatio-temporal~~spatiotemporal matching of the SEVIRI pixels with the METAR locations, heterogeneity of the land surface topography and sky condition at the subpixel level, and the ~~difference~~differences in the measurement devices and calibration standards used ~~in generating~~to generate the METAR observations. ~~Nevertheless~~However, the encouraging results obtained ~~in the present study~~ show that the spatio-temporal matching of ~~both~~ SEVIRI and METAR datasets ~~in this study~~ has been ~~very good,~~effective and the pre-processing ~~methods~~procedure applied ~~have~~here successfully screened out many of the ambiguous situations.

In summary, the FLS detection algorithm developed here is accurate and ~~as it can be applied~~applicable over the 24H cycle of the day~~ it can provide~~, providing new insights to FLS studies and ~~enable~~enabling the development of existing/new FLS fore-/now-casting techniques. The positive results obtained here, and the potential of the algorithm ~~encourages an expansion~~encourage the extension of the validation to other regions ~~covered~~observed by the SEVIRI instrument. Ideally, the algorithm presented here ~~could also~~can be further developed to discriminate between fog and low stratus, detect FLS layers that are placed underneath optically thin non-FLS-clouds, or/and differentiate snow-covered ~~and~~from snow-free lands ~~from each other~~.

610 **Appendix A: workflow followed for the creation of the training and testing datasets.**

Figure A1 schematically describes the process followed in Sect. 2 for creation of the MFL (Modified FLS Labels) included the datasets "~~train~~training", "$test_1$", "$test_2$", "$test_3$", and "$test_4$".

Formatted: Centered

All 947 METAR Stations

Quality Control — fail → 591 stations

pass

356 stations

HV, CBH, CC — unavailable → undefined

Spatial and Temporal Matching with SEVIRI

Raw FLS labels (FLS, No FLS)

$P_{6.2}$, $P_{7.3}$, $BT_{8.7}$, $BT_{10.8}$, $BT_{12.0}$ and $BT_{13.4}$

High Cloud? — unavailable → undefined

Modified FLS labels (MFL): (Clear-sky, FLS, High cloud, Multilayer)

Annual frequency of FLS occurrence (f)

Period
2016-2017
2017-2018
2019-2020
2020-2021
2018-2019
2021-2022

f — 21 stations ... 276 stations

59 stations

Period
2016-2017
2017-2018
2019-2020
2020-2021
2018-2019
2021-2022

te_2 datasets | te_3 datasets | $s\ te_4$ dataset as | $test_1$ dataset | $tr\ in$ dataset

Label Confidence Evaluation

Confident? — No → discard ← No — Confident?

Yes

Multi-layer conditions relabeled as high cloud

Multi-layer conditions removed

Final test MFL (Clear-sky, FLS, High cloud)

te_2 datasets | $test_3$ datasets | $s\ te_4$ dataset | $s\ te_1$ dataset

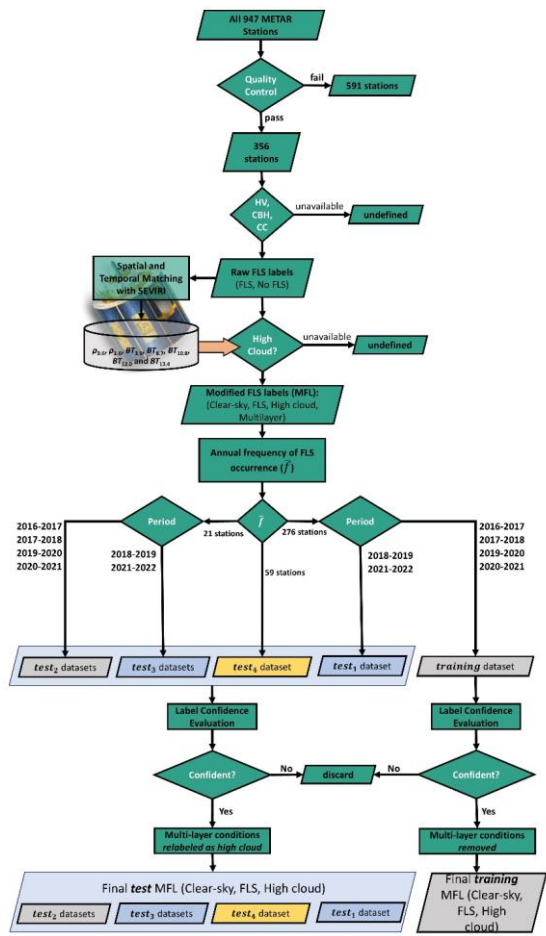Final train MFL (Clear-sky, FLS, High cloud)

615 **Figure A1. Schematic description of the process followed in Sect. 2 for creation of the MFL (Modified FLS Labels) included the datasets "~~train~~training", "test₁", "test₂", "test₃", and "test₄".**

Appendix B: Equations of statistical validation metrics

$$POD = N_{TP} / (N_{TP} + N_{FN}) \tag{B1}$$

$$FAR = N_{FP} / (N_{TP} + N_{FP}) \tag{B2}$$

$$PFD = N_{TN} / (N_{FP} + N_{TN}) \tag{B3}$$

$$CSI = N_{TP} / (N_{TP} + N_{FN} + N_{FP}) \tag{B4}$$

$$ACC = (N_{TP} + N_{TN}) / (N_{TP} + N_{TN} + N_{FP} + N_{FN}) \tag{B5}$$

$$BS = (N_{TP} + N_{FP}) / (N_{TP} + N_{FN}) \tag{B6}$$

$$d = ((POD\text{-}1)^2 + FAR^2)^{0.5} \tag{B7}$$

where N_{TP}, N_{FN}, N_{FP}, and N_{TN}, respectively, are the number of *true positives*, *false negatives*, *false positives*, and *true negatives*, as described in Table B1. *POD* quantifies the skill of the method in correctly identifying the FLS cases. *FAR* indicates the portion of false alarms among all the cases classified as FLS by the algorithm. *PFD* highlights the portion of the non-FLS cases which have been correctly classified as non-FLS by the algorithm. *CSI* is a metric indicating the overall correctness of the FLS classification. *ACC* shows the portion of the cases which have been correctly identified as FLS and non-FLS. The metrics *POD*, *FAR*, *PFD*, *CSI*, and *ACC* vary between 0 and 1. An ideal detection algorithm should have a *POD*, *PFD*, *CSI*, and *ACC* equal to 1, and *FAR* equal to 0. *BS* reflects the overall bias of the product. *BS* varies in between 0 and $+\infty$, with the optimal value being 1. The values of *BS* greater and smaller than 1 reflect over- and under-estimation of the FLS class, respectively. As can be inferred from Eq. (6), *d* is a metric obtained by combining the statistical indicators *POD* and *FAR* and compares the performance of the algorithm with the ideal algorithm (*FAR: 0, POD: 1*). In other words, it indicates how distant the performance of the FLS detection algorithm is in comparison with that of the best algorithm which can ideally exist. *d* varies between 0 and $\sqrt{2}$, with 0 being the ideal value.

Table B 1. Confusion matrix, explaining how the *true positives*, *false negatives*, *false positives*, and *true negatives* are determined.

		Truth (MFL)	
		FLS	Not FLS
Product	FLS	True Positive (TP)	False Positive (FP)
	Not FLS	False Negative (FN)	True Negative (TN)

27

Code availability

The python implementations of SOFOS and the FLS detection model developed here can be provided upon request. The source codes for the XGBoost python implementations used in the present study can be freely obtained from https://xgboost.readthedocs.io/en/stable/index.html, last access: 13.10.2023. The satpy python package can be freely accessed from https://satpy.readthedocs.io/en/stable/, last access: 13.10.2023.

Data availability

All the raw data used in the present study are publicly available, and details on the datasets are provided in Sect. 2. The Supplement animation S1 can be downloaded from https://doi.org/10.5281/zenodo.10244714. MSG-SEVIRI data used in this study were provided by EUMETSAT (European Organization for the Exploitation of Meteorological Satellites) and can be accessed via https://www.eumetsat.int/access-our-data, last access: 22.12.2023. The elevation map used in Figure 1 was obtained from the EUMETSAT LSA-SAF (Satellite Application Facility on Land Surface Analysis) auxiliary data at https://lsa-saf.eumetsat.int/en/user-support/auxiliary-data/, last access: 16.01.2023. METAR data used in the present study were obtained from https://mesonet.agron.iastate.edu/request/download.phtml, last access: 10.12.2022.

Author contribution

All authors contributed to the review of the manuscript. JC, JF, and SK contributed to the conceptualization of the project. JF, SK, JC and TZ contributed to the design of the study and interpretation of the results. JF contributed to the project administration. MZ downloaded and organized the raw SEVIRI dataoperated and applied the SOFOS algorithm to them.raw SEVIRI data. BJ and SK generated of the label data. BJ contributed to the design of the study, performed the computations, interpreted the results and wrote the manuscript. All authors contributed to the review and editing of the manuscript.

Competing interests

The contact author has declared that none of the authors has anydeclare no competing interests.

Formatted: Centered

References

Aminou, D. M. A. (2002). MSG 's SEVIRI Instrument. *ESA Bulletin*, 15–17.

Andersen, H., & Cermak, J. (2018). First fully diurnal fog and low cloud satellite detection reveals life cycle in the Namib. *Atmospheric Measurement Techniques*, *11*(10), 5461–5470. https://doi.org/10.5194/amt-11-5461-2018

Cermak, J. (2006). SOFOS – A New Satellite-based Operational Fog Observation Scheme. *PhD Thesis, Philipps-Universität Marburg, March.* http://archiv.ub.uni-marburg.de/diss/z2006/0149/

Cermak, J., & Bendix, J. (2007). Dynamical nighttime fog/low stratus detection based on Meteosat SEVIRI data: A feasibility study. *Pure and Applied Geophysics*, *164*(6–7), 1179–1192. https://doi.org/10.1007/s00024-007-0213-8

Cermak, J., & Bendix, J. (2008). A novel approach to fog/low stratus detection using Meteosat 8 data. *Atmospheric Research*, *87*(3–4), 279–292. https://doi.org/10.1016/j.atmosres.2007.11.009

Cermak, J., Eastman, R. M., Bendixc, J., & Warrenb, S. G. (2009). European climatology of fog and low stratus based on geostationary satellite observations. *Quarterly Journal of the Royal Meteorological Society*, *135*, 2125–2130. https://doi.org/10.1002/qj

Egli, S., Thies, B., Drönner, J., Cermak, J., & Bendix, J. (2017). A 10 year fog and low stratus climatology for Europe based on Meteosat Second Generation data. *Quarterly Journal of the Royal Meteorological Society*, *143*(702), 530–541. https://doi.org/10.1002/qj.2941

Egli, S., Thies, S., & Bendix, J. (2018). A hybrid approach for fog retrieval based on a combination of satellite and ground truth data. *Remote Sensing*, *10*(4). https://doi.org/10.3390/rs10040628

Ellrod, G. P. (1995). Advances in the Detection and Analysis of Fog at Night Using GOES Multispectral Infrared Imagery. *Weather and Forecasting*, *10*(3), 606–619. https://doi.org/https://doi.org/10.1175/1520-0434(1995)010%3C0606:AITDAA%3E2.0.CO;2

EUMETSAT. (2017). MSG Level 1.5 Image Data Format Description. In *EUMETSAT* (p. 127). https://www.eumetsat.int/media/45126

Friedman, J. H. (2001). Greedy function approximation: A gradient boosting machine. *Annals of Statistics*, *29*(5), 1189–1232. https://doi.org/10.1214/aos/1013203451

Güls, I., & Bendix, J. (1996). Fog detection and fog mapping using low cost Meteosat-WEFAX transmission. *Meteorological Applications*, *3*(2), 179–187. https://doi.org/10.1002/met.5060030208

Hanson, C., & Mueller, J. (2004). Status of the SEVIRI level 1.5 data. *European Space Agency, (Special Publication) ESA SP*, *582*, 17–21.

Hunt, G. E. (1973). Radiative properties of terrestrial clouds at visible and infra-red thermal window wavelengths. *Quarterly Journal of the Royal Meteorological Society*, *99*(420), 346–369. https://doi.org/10.1002/qj.49709942013

Jahani, B., Andersen, H., Calbo, J., Gonzalez, J. A., & Cermak, J. (2022). Longwave radiative effect of the cloud-aerosol transition zone based on CERES observations. *Atmospheric Chemistry and Physics*, *22*(2), 1483–1494. https://doi.org/10.5194/acp-22-1483-2022

Jahani, B., Calbó, J., & González, J. A. (2020). Quantifying Transition Zone Radiative Effects in Longwave Radiation Parameterizations. *Geophysical Research Letters*, *47*(22), e2020GL090408. https://doi.org/https://doi.org/10.1029/2020GL090408

Kim, S. H., Suh, M. S., & Han, J. H. (2019). Development of Fog Detection Algorithm during Nighttime Using Himawari-8/AHI Satellite and Ground Observation Data. *Asia-Pacific Journal of Atmospheric Sciences*, *55*(3), 337–350. https://doi.org/10.1007/s13143-018-0093-0

Köhler, C., Steiner, A., Saint-Drenan, Y. M., Ernst, D., Bergmann-Dick, A., Zirkelbach, M., Ben Bouallègue, Z., Metzinger, I., & Ritter, B. (2017). Critical weather situations for renewable energies – Part B: Low stratus risk for solar power. *Renewable Energy*, *101*, 794–803. https://doi.org/10.1016/j.renene.2016.09.002

Koren, I., Remer, L. A., Kaufman, Y. J., Rudich, Y., & Martins, J. V. (2007). On the twilight zone between clouds and aerosols. *Geophysical Research Letters*, *34*(8), 1–5. https://doi.org/10.1029/2007GL029253

Lee, J. R., Chung, C. Y., & Ou, M. L. (2011). Fog detection using geostationary satellite data: Temporally continuous algorithm. *Asia-Pacific Journal of Atmospheric Sciences*, *47*(2), 113–122. https://doi.org/10.1007/s13143-011-0002-2

Lehnert, L. W., Thies, B., Trachte, K., Achilles, S., Osses, P., Baumann, K., Schmidt, J., Samolov, E., Jung, P., Leinweber, P., Karsten, U., Büdel, B., & Bendix, J. (2018). A Case Study on Fog/Low Stratus Occurrence at Las Lomitas, Atacama Desert (Chile) as a Water Source for Biological Soil Crusts. *Aerosol and Air Quality Research*, *18*(1), 226–254. https://doi.org/10.4209/aaqr.2017.01.0021

Martin, R., David, H., Panu, L., Stephan, F., Gerrit, H., Adam, D., Simon, P., Andrea, M., Xin, Z., Sauli, J., Joleen, F., William, R., Lars, Ø. R., Jorge, H. B. M., Yufei, Z., BENR0, Strandgren, Rohan, D., Tommy, J., … Jkotro. (2021). *pytroll/satpy: Version 0.29.0 (v0.29.0)*. Zenodo. https://doi.org/https://doi.org/10.5281/zenodo.4904606

Mitchell, R., & Frank, E. (2017). Accelerating the XGBoost algorithm using GPU computing. *PeerJ Computer Science*, *2017*(7). https://doi.org/10.7717/peerj-cs.127

Natekin, A., & Knoll, A. (2013). Gradient boosting machines, a tutorial. *Frontiers in Neurorobotics*, *7*(DEC). https://doi.org/10.3389/fnbot.2013.00021

Nilo, S. T., Romano, F., Cermak, J., Cimini, D., Ricciardelli, E., Cersosimo, A., Di Paola, F., Gallucci, D., Gentile, S., Geraldi, E., Larosa, S., Ripepi, E., & Viggiano, M. (2018). Fog detection based on Meteosat Second Generation-Spinning enhanced visible and infrared imager high resolution visible channel. *Remote Sensing*, *10*(4), 1–20. https://doi.org/10.3390/rs10040541

Pauli, E., Cermak, J., & Andersen, H. (2022). A satellite-based climatology of fog and low stratus formation and dissipation times in central Europe. *Quarterly Journal of the Royal Meteorological Society*, *148*(744), 1439–1454. https://doi.org/10.1002/qj.4272

Pauli, E., Cermak, J., & Teuling, A. J. (2022). Enhanced Nighttime Fog and Low Stratus Occurrence Over the Landes Forest, France. *Geophysical Research Letters*, *49*(5), 1–9. https://doi.org/10.1029/2021GL097058

Pérez Díaz, J. L., Ivanov, O., Peshev, Z., álvarez-Valenzuela, M. A., Valiente-Blanco, I., Evgenieva, T., Dreischuh, T., Gueorguiev, O., Todorov, P. V., & Vaseashta, A. (2017). Fogs: Physical basis, characteristic properties, and impacts on the environment and human health. *Water (Switzerland)*, *9*(10), 1–21. https://doi.org/10.3390/w9100807

Schmetz, J., Pili, P., Tjemkes, S., Just, D., Kermann, J., Rota, S., & Ratier, A. (2002). Seviri calibration. *Bulletin of the American Meteorological Society*, *83*(7), ES52–ES53.

Shanyengana, E. S., Henschel, J. R., Seely, M. K., & Sanderson, R. D. (2002). Exploring fog as a supplementary water source in Namibia. *Atmospheric Research*, *64*(1), 251–259. https://doi.org/https://doi.org/10.1016/S0169-8095(02)00096-0

Tranquilli, C., Viticchiè, B., Pessina, S., Hewison, T., Müller, J., & Wagner, S. (2016). Meteosat SEVIRI performance characterisation and calibration with dedicated Moon/Sun/deep-space scans. *14th International Conference on Space Operations, 2016*. https://doi.org/10.2514/6.2016-2536

Underwood, S. J., Ellrod, G. P., & Kuhnert, A. L. (2004). A multiple-case analysis of nocturnal radiation-fog development in the Central Valley of California utilizing the GOES nighttime fog product. *Journal of Applied Meteorology*, *43*(2), 297–311. https://doi.org/10.1175/1520-0450(2004)043<0297:AMAONR>2.0.CO;2

Vautard, R., Yiou, P., & Van Oldenborgh, G. J. (2009). Decline of fog, mist and haze in Europe over the past 30 years. *Nature Geoscience*, *2*(2), 115–119. https://doi.org/10.1038/ngeo414 Aminou, D. M. A.: MSG 's SEVIRI Instrument, ESA Bull., 15–17, 2002.

Andersen, H. and Cermak, J.: First fully diurnal fog and low cloud satellite detection reveals life cycle in the Namib, Atmos. Meas. Tech., 11, 5461–5470, https://doi.org/10.5194/amt-11-5461-2018, 2018.

Cermak, J.: SOFOS -- A New Satellite-based Operational Fog Observation Scheme, PhD Thesis, Philipps-Universität Marbg., 2006.

Cermak, J.: Fog and Low Cloud Frequency and Properties from Active-Sensor Satellite Data, Remote Sens., 10, 1209, https://doi.org/10.3390/rs10081209, 2018.

Cermak, J. and Bendix, J.: Dynamical nighttime fog/low stratus detection based on Meteosat SEVIRI data: A feasibility study, Pure Appl. Geophys., 164, 1179–1192, https://doi.org/10.1007/s00024-007-0213-8, 2007.

Cermak, J. and Bendix, J.: A novel approach to fog/low stratus detection using Meteosat 8 data, Atmos. Res., 87, 279–292, https://doi.org/10.1016/j.atmosres.2007.11.009, 2008.

Cermak, J., Eastman, R. M., Bendixc, J., and Warrenb, S. G.: European climatology of fog and low stratus based on geostationary satellite observations, Q. J. R. Meteorol. Soc., 135, 2125–2130, https://doi.org/10.1002/qj, 2009.

Egli, S., Thies, B., Drönner, J., Cermak, J., and Bendix, J.: A 10 year fog and low stratus climatology for Europe based on Meteosat Second Generation data, Q. J. R. Meteorol. Soc., 143, 530–541, https://doi.org/10.1002/qj.2941, 2017.

Egli, S., Thies, S., and Bendix, J.: A hybrid approach for fog retrieval based on a combination of satellite and ground truth data, Remote Sens., 10, https://doi.org/10.3390/rs10040628, 2018.

Ellrod, G. P.: Advances in the Detection and Analysis of Fog at Night Using GOES Multispectral Infrared Imagery, Weather Forecast., 10, 606–619, https://doi.org/https://doi.org/10.1175/1520-0434(1995)010%3C0606:AITDAA%3E2.0.CO;2, 1995.

EUMETSAT: MSG Level 1.5 Image Data Format Description, https://www.eumetsat.int/media/45126, 2017.

Friedman, J. H.: Greedy function approximation: A gradient boosting machine, Ann. Stat., 29, 1189–1232, https://doi.org/10.1214/aos/1013203451, 2001.

Güls, I. and Bendix, J.: Fog detection and fog mapping using low cost Meteosat-WEFAX transmission, Meteorol. Appl., 3, 179–187, https://doi.org/10.1002/met.5060030208, 1996.

Hanson, C. and Mueller, J.: Status of the SEVIRI level 1.5 data, Eur. Sp. Agency, (Special Publ. ESA SP, 17–21, 2004.

Hunt, G. E.: Radiative properties of terrestrial clouds at visible and infra-red thermal window wavelengths, Q. J. R. Meteorol. Soc., 99, 346–369, https://doi.org/10.1002/qj.49709942013, 1973.

Jahani, B., Calbó, J., and González, J. A.: Quantifying Transition Zone Radiative Effects in Longwave Radiation Parameterizations, Geophys. Res. Lett., 47, e2020GL090408, https://doi.org/https://doi.org/10.1029/2020GL090408, 2020.

Jahani, B., Andersen, H., Calbo, J., Gonzalez, J. A., and Cermak, J.: Longwave radiative effect of the cloud-aerosol transition zone based on CERES observations, Atmos. Chem. Phys., 22, 1483–1494, https://doi.org/10.5194/acp-22-1483-2022, 2022.

Kim, S. H., Suh, M. S., and Han, J. H.: Development of Fog Detection Algorithm during Nighttime Using Himawari-8/AHI Satellite and Ground Observation Data, Asia-Pacific J. Atmos. Sci., 55, 337–350, https://doi.org/10.1007/s13143-018-0093-0, 2019.

Köhler, C., Steiner, A., Saint-Drenan, Y. M., Ernst, D., Bergmann-Dick, A., Zirkelbach, M., Ben Bouallègue, Z., Metzinger, I., and Ritter, B.: Critical weather situations for renewable energies – Part B: Low stratus risk for solar power, Renew. Energy, 101, 794–803, https://doi.org/10.1016/j.renene.2016.09.002, 2017.

Koren, I., Remer, L. A., Kaufman, Y. J., Rudich, Y., and Martins, J. V.: On the twilight zone between clouds and aerosols, Geophys. Res. Lett., 34, 1–5, https://doi.org/10.1029/2007GL029253, 2007.

Lee, J. R., Chung, C. Y., and Ou, M. L.: Fog detection using geostationary satellite data: Temporally continuous algorithm, Asia-Pacific J. Atmos. Sci., 47, 113–122, https://doi.org/10.1007/s13143-011-0002-2, 2011.

Lehnert, L. W., Thies, B., Trachte, K., Achilles, S., Osses, P., Baumann, K., Schmidt, J., Samolov, E., Jung, P., Leinweber, P., Karsten, U., Büdel, B., and Bendix, J.: A Case Study on Fog/Low Stratus Occurrence at Las Lomitas, Atacama Desert (Chile) as a Water Source for Biological Soil Crusts, Aerosol Air Qual. Res., 18, 226–254, https://doi.org/10.4209/aaqr.2017.01.0021, 2018.

Martin, R., David, H., Panu, L., Stephan, F., Gerrit, H., Adam, D., Simon, P., Andrea, M., Xin, Z., Sauli, J., Joleen, F., William, R., Lars, Ø. R., Jorge, H. B. M., Yufei, Z., BENR0, Strandgren, Rohan, D., Tommy, J., …, and Jkotro: pytroll/satpy: Version 0.29.0 (v0.29.0), https://doi.org/https://doi.org/10.5281/zenodo.4904606, 2021.

Mitchell, R. and Frank, E.: Accelerating the XGBoost algorithm using GPU computing, PeerJ Comput. Sci., 2017, https://doi.org/10.7717/peerj-cs.127, 2017.

Natekin, A. and Knoll, A.: Gradient boosting machines, a tutorial, Front. Neurorobot., 7,

https://doi.org/10.3389/fnbot.2013.00021, 2013.

Nilo, S. T., Romano, F., Cermak, J., Cimini, D., Ricciardelli, E., Cersosimo, A., Di Paola, F., Gallucci, D., Gentile, S., Geraldi, E., Larosa, S., Ripepi, E., and Viggiano, M.: Fog detection based on Meteosat Second Generation-Spinning enhanced visible and infrared imager high resolution visible channel, Remote Sens., 10, 1–20, https://doi.org/10.3390/rs10040541, 2018.

Pauli, E., Cermak, J., and Andersen, H.: A satellite-based climatology of fog and low stratus formation and dissipation times in central Europe, Q. J. R. Meteorol. Soc., 148, 1439–1454, https://doi.org/10.1002/qj.4272, 2022a.

Pauli, E., Cermak, J., and Teuling, A. J.: Enhanced Nighttime Fog and Low Stratus Occurrence Over the Landes Forest, France, Geophys. Res. Lett., 49, 1–9, https://doi.org/10.1029/2021GL097058, 2022b.

Pérez-Díaz, J. L., Ivanov, O., Peshev, Z., álvarez-Valenzuela, M. A., Valiente-Blanco, I., Evgenieva, T., Dreischuh, T., Gueorguiev, O., Todorov, P. V., and Vaseashta, A.: Fogs: Physical basis, characteristic properties, and impacts on the environment and human health, 9, 1–21, https://doi.org/10.3390/w9100807, 2017.

Petitcolin, F. and Vermote, E.: Land surface reflectance, emissivity and temperature from MODIS middle and thermal infrared data, Remote Sens. Environ., 83, 112–134, https://doi.org/https://doi.org/10.1016/S0034-4257(02)00094-9, 2002.

Schmetz, J., Pili, P., Tjemkes, S., Just, D., Kermann, J., Rota, S., and Ratier, A.: Seviri calibration, Bull. Am. Meteorol. Soc., 83, ES52–ES53, 2002.

Shanyengana, E. S., Henschel, J. R., Seely, M. K., and Sanderson, R. D.: Exploring fog as a supplementary water source in Namibia, Atmos. Res., 64, 251–259, https://doi.org/https://doi.org/10.1016/S0169-8095(02)00096-0, 2002.

Strabala, K. I., Ackerman, S. A., and Menzel, W. P.: Cloud properties inferred from 8-12-μm data, J. Appl. Meteorol., 33, 212–229, https://doi.org/10.1175/1520-0450(1994)033<0212:CPIFD>2.0.CO;2, 1994.

Tranquilli, C., Viticchiè, B., Pessina, S., Hewison, T., Müller, J., and Wagner, S.: Meteosat SEVIRI performance characterisation and calibration with dedicated Moon/Sun/deep-space scans, in: 14th International Conference on Space Operations, 2016, https://doi.org/10.2514/6.2016-2536, 2016.

Underwood, S. J., Ellrod, G. P., and Kuhnert, A. L.: A multiple-case analysis of nocturnal radiation-fog development in the Central Valley of California utilizing the GOES nighttime fog product, J. Appl. Meteorol., 43, 297–311, https://doi.org/10.1175/1520-0450(2004)043<0297:AMAONR>2.0.CO;2, 2004.

Vautard, R., Yiou, P., and Van Oldenborgh, G. J.: Decline of fog, mist and haze in Europe over the past 30 years, Nat. Geosci., 2, 115–119, https://doi.org/10.1038/ngeo414, 2009.

Formatted: Centered